

Appendix A

Toward Higher Accuracy: A CDM Example

The scale invariant cold dark matter (CDM) model with $\Omega_0 = 1.0$ and $\Omega_b h^2$ near the nucleosynthesis value $\Omega_b h^2 \simeq 0.01 - 0.02$ is elegantly simple and succeeds in explaining the gross features of both anisotropies in the CMB and large scale structure formation. It is therefore of value to study this model more closely. We will here refine our understanding of primary anisotropy formation first to the 5% level down to a fraction of a degree. It is possible and instructive to carry out this task through analytic construction. We then embark on the quest of obtaining 1% accurate results through the arcminute scale by considering the numerical calculation of subtle effects. This treatment should serve as an example of the types of consideration necessary for accurate predictions in the general case.

Aside from the coupling to the baryons, photons only experience gravitational effects from the other matter components. Primary anisotropy formation therefore depends sensitively on two quantities

1. The evolution of the metric perturbations.
2. The decoupling of the photons from the baryons.

We must therefore refine our understanding of both. As for the metric perturbations Ψ and Φ , there are two modifications we must make to the analysis of §5.1 and §5.2. At large scales we must include the anisotropic stress contribution of the neutrinos. Anisotropic stress

serves to differentiate the Newtonian potential Ψ from the space curvature perturbation Φ . As we have seen in §6, they are both important in anisotropy formation. At small scales, we must be able to describe accurately the pressure feedback effects from the radiation onto the potentials. This in turn leads to some sensitivity to neutrino masses in the eV range. Finally, tensor metric perturbations, *i.e.* gravity waves, can also produce gravitational redshifts and dilation in the CMB. Depending on the exact inflationary model, they can perhaps be significant at large scales but are almost certainly small perturbations to the scalar spectrum near the acoustic peaks. We shall quantify this statement in section A.3.3.

We must also improve our understanding of recombination over the equilibrium Saha treatment presented in §6.3.4. Last scattering is delayed due to the high opacity to recombination photons which keep the plasma ionized [123, 183]. This delay increases the diffusion length and thus is responsible for further damping of anisotropies. Following the population of the first excited state of hydrogen allows analytic construction of the anisotropies to 5% through to the damping scale. Subtle effects can change the damping scale at the several percent level. Polarization feedback weakens photon-baryon coupling by generating viscosity, *i.e.* a quadrupole moment in the photons. Helium ionization decreases the diffusion length before helium recombination. It is quite possible that other subtle effects change the damping tail at a comparable or even greater level. We offer these two considerations only as examples of the care that is required to obtain 1% accurate primary anisotropies under the damping scale.

A.1 Refining the Gravitational Potentials

A.1.1 Neutrino Anisotropic Stress

The solution for the gravitational potentials given by equation (5.11) must be corrected for the anisotropic stress Π_T . Recall that the anisotropic stress is related to the quadrupole moments of the radiation via equation (4.55), *i.e.*

$$p_T \Pi_T = \frac{12}{5} (p_\gamma \Theta_2 + p_\nu N_2). \quad (\text{A.1})$$

Due to the isotropizing effects of scattering, the anisotropic stress of the photons is negligibly small before recombination. Hence the main contribution to Π_T comes from the neutrino quadrupole anisotropy N_2 .

We can take it into account perturbatively. Specifically, we use the exact zeroth order growing and decaying solutions (5.11) to obtain the anisotropic stress. We then take this solution to iteratively correct for anisotropic stress in the evolution equation (5.6). If we neglect higher order multipole components, which is reasonable for superhorizon sized modes, the second moment of the Boltzmann equation (4.54) for the neutrinos becomes

$$\dot{N}_2 = \frac{2}{3}kN_1 \simeq \frac{2}{3}kV_T, \quad (\text{A.2})$$

where recall from §5.1.1 that all fluid velocities are equal above the horizon *i.e.* $N_1 \equiv V_\nu \simeq V_T$.

The exact zeroth order solution for V_T is found by substituting the growing mode solution equation (5.11) into the continuity equation (5.24). If the zeroth order solution is denoted $\Delta_T = C_G U_G$, then the solution to equation (A.2) is

$$\bar{N}_2(a)/C_G \simeq 2 \int_0^a \frac{da'}{a'} \frac{1}{3a'+4} \left(U_G - (a'+1)a' \frac{dU_G}{da'} \right), \quad (\text{A.3})$$

where recall that $3w_T = 1/(1+a)$ with a normalized at equality. The overbar represents the superhorizon solution since pressure growth suppression inside the horizon must be taken into account (see §A.1.2). Although it is possible to analytically integrate equation (A.3), the expression is cumbersome. Instead, we can employ an approximate solution which is exact in the limit $a \ll 1$ and $a \gg 1$,

$$\bar{N}_2(a)/C_G = -\frac{1}{10} \frac{20a+19}{3a+4} U_G - \frac{8}{3} \frac{a}{3a+4} + \frac{8}{9} \ln \left(\frac{3a+4}{4} \right). \quad (\text{A.4})$$

We have checked that this approximation works quite well by comparing it to equation (A.3) and the full numerical solution.

Next, we employ the above solution for \bar{N}_2 in equations (5.6). These two first order equations may be rewritten as one second order equation for Δ_T . The particular solution including the source terms Π_T and $\dot{\Pi}_T$ can be obtained from the homogeneous solutions U_G and U_D by Green's method,

$$\bar{\Delta}_T(a)/C_G = \left(1 + \frac{2}{5}f_\nu \right) U_G(a) + \frac{2}{5}f_\nu [I_1(a)U_G(a) + I_2(a)U_D(a)], \quad (\text{A.5})$$

where $I_1(a) = \int_0^a da' F_\nu(a') U_D(a')$, $I_2(a) = \int_0^a da' F_\nu(a') U_G(a')$,

$$F_\nu(a) = \frac{24}{5} \frac{(a+1)^{5/2}}{a^2(3a+4)} \left\{ \frac{2a}{3a+4} \frac{d}{da} U_G(a) - \frac{2}{(3a+4)(a+1)} U_G(a) + \left[\frac{1}{(a+1)^2} - \frac{2}{a+1} + \frac{12}{3a+4} \right] \bar{N}_2(a)/C_G \right\}, \quad (\text{A.6})$$

and recall f_ν is the ratio of neutrino to total radiation density $f_\nu \equiv \rho_\nu/(\rho_\nu + \rho_\gamma)$. If we assume three massless neutrinos and the standard thermal history, $\rho_\nu/\rho_\gamma = 3(7/4)(4/11)^{4/3}/2 = 0.68$, *i.e.* $f_\nu = 0.405$. The first term in equation (A.5) comes from the initial conditions for Δ_T which can be iteratively established by employing equation (A.2) in (5.6). All terms which are proportional to f_ν in the equation (A.5) come from equation (A.1) since the anisotropic stress $\Pi_T \simeq (12/5)f_\nu N_2$. The asymptotic behavior of equation (A.5) is

$$\bar{\Delta}_T(a) \rightarrow \begin{cases} \left(1 + \frac{2}{5}f_\nu\right) C_G U_G(a) & (a \ll 1) \\ \left(1 + \frac{4}{15}f_\nu\right) C_G U_G(a). & (a \gg 1) \end{cases} \quad (\text{A.7})$$

Here we have used the fact that if $a \gg 1$, the decaying term $I_2 U_D$ may be ignored and $I_1 \rightarrow -\frac{1}{3}$ approximately.

Therefore we may obtain a simple approximate expression for the large scale density fluctuations,

$$\bar{\Delta}_T(a) \simeq \left[1 + \frac{2}{5}f_\nu \left(1 - \frac{1}{3} \frac{a}{a+1}\right)\right] C_G U_G(a). \quad (\text{A.8})$$

Again we have checked that this approximation works reasonably well by comparing it to numerical calculations. The potentials $\bar{\Phi}$ and $\bar{\Psi}$ are therefore written as

$$\begin{aligned} \bar{\Phi}(a) &= \frac{3}{4} \left(\frac{k_{eq}}{k}\right)^2 \frac{a+1}{a^2} \bar{\Delta}_T(a), \\ \bar{\Psi}(a) &= -\frac{3}{4} \left(\frac{k_{eq}}{k}\right)^2 \frac{a+1}{a^2} \left(\bar{\Delta}_T(a) + \frac{8}{5}f_\nu \frac{\bar{N}_2(a)}{a+1}\right), \end{aligned} \quad (\text{A.9})$$

where recall $k_{eq} = \sqrt{2}(\Omega_0 H_0^2 a_0)^{1/2}$ is the scale that passes the horizon at matter-radiation equality. By using the asymptotic form of $\bar{\Delta}_T$ and \bar{N}_2 , we easily obtain the corresponding relation between $\bar{\Phi}$ and $\bar{\Psi}$,

$$\bar{\Phi}(a) = \begin{cases} -\bar{\Psi}(a) \left(1 + \frac{2}{5}f_\nu\right) & (a \ll 1) \\ -\bar{\Psi}(a). & (a \gg 1) \end{cases} \quad (\text{A.10})$$

Also of interest are the ratios of initial to final values of the gravitational potentials:

$$\begin{aligned} \bar{\Phi}(a_0) &= -\bar{\Psi}(a_0) = \frac{9}{10} \left(1 + \frac{4}{15}f_\nu\right) \left(1 + \frac{2}{5}f_\nu\right)^{-1} \bar{\Phi}(0), \\ \bar{\Psi}(a_0) &= \frac{9}{10} \left(1 + \frac{4}{15}f_\nu\right) \bar{\Psi}(0). \end{aligned} \quad (\text{A.11})$$

Thus we see that the correction for anisotropic stress makes a 10% difference in $\bar{\Psi}$ during radiation domination. If recombination occurs near equality, this results in a small correction to the standard Sachs-Wolfe formula due to anisotropic stress.

The initial conditions for the perturbations may now be expressed in terms of $\bar{\Phi}(0)$,

$$\begin{aligned}\Psi(0) &\equiv \bar{\Psi}(0) = -\left(1 + \frac{2}{5}f_\nu\right)^{-1} \bar{\Phi}(0), \\ \Theta(0) &\equiv \bar{\Theta}(0) = \frac{1}{2}\left(1 + \frac{2}{5}f_\nu\right)^{-1} \bar{\Phi}(0).\end{aligned}\tag{A.12}$$

Note that since all modes are superhorizon sized at the initial epoch, the overbar is superfluous. Moreover, even in the initial conditions, the anisotropic stress represents a small but important correction to the $\Pi_T = 0$ solutions of §5.1, $\bar{\Phi}(0) = -\bar{\Psi}(0) = 2\bar{\Theta}_0(0)$. Finally, we can relate these quantities to the initial power spectrum,

$$k^3|\Phi(0, k)|^2 \equiv k^3|\bar{\Phi}(0, k)|^2 = \left[\frac{5}{6}\left(1 + \frac{2}{5}f_\nu\right)\right]^2 \left(\frac{k_{eq}}{k}\right)^4 k^3 C_G^2(k) = Bk^{n-1},\tag{A.13}$$

where we have restored the implicit k index. Note that C_G is the normalization of the density fluctuations at equality. It is related to the matter power spectrum today $|\Delta(\eta_0, k)|^2 = Ak^n$ by

$$\begin{aligned}Ak^n &\simeq \left[\left(1 + \frac{4}{15}f_\nu\right) C_G a_0/a_{eq}\right]^2 \\ &\simeq \left(1 + \frac{4}{15}f_\nu\right)^2 \left(1 + \frac{2}{5}f_\nu\right)^{-2} \frac{36}{25} k_{eq}^{-4} (a_0/a_{eq})^2 Bk^n \\ &\simeq \left(1 + \frac{4}{15}f_\nu\right)^2 \left(1 + \frac{2}{5}f_\nu\right)^{-2} \frac{9}{25} (\Omega_0 H_0^2)^{-2} Bk^n,\end{aligned}\tag{A.14}$$

[*c.f.* equation (6.12)] where we have used equation (A.8).

A.1.2 Small Scale Radiation Feedback

Next we need to obtain solutions of Ψ and Φ in the small scale limit where pressure cannot be neglected. Qualitatively speaking, we know that the potentials decay inside the sound horizon in the radiation-dominated epoch since pressure prevents Δ_T from growing. However in general, it is impossible to obtain the exact solution valid through matter-radiation equality even if we neglect the anisotropic stress term. Only the asymptotic behavior in certain limits has been found [101]. For the CDM scenario, it is well known that the *final* value of the potential at small scales is obtained from the superhorizon solution (A.9) by the transfer function $\Phi(a_0) = -\Psi(a_0) = T(k)\bar{\Phi}(a_0)$, where

$$T(k) = \frac{\ln(1 + 2.34q)}{2.34q} [1 + 3.89q + (14.1q)^2 + (5.46q)^3 + (6.71q)^4]^{-1/4},\tag{A.15}$$

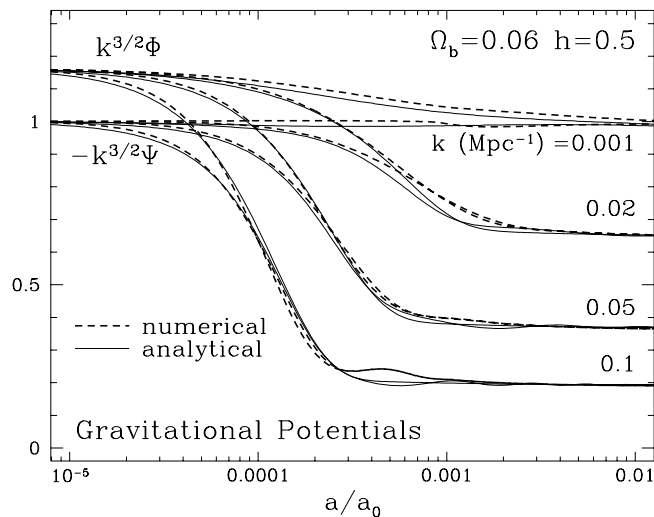


Figure A.1: Gravitational Potential Evolution

Gravitational potentials in the Harrison-Zel'dovich CDM model. The potential decays after crossing the sound horizon in the radiation dominated epoch and only flattens out *well* into the matter dominated epoch. Moreover $\Phi \neq -\Psi$ early on due to anisotropic stress. The analytic approximations trace the numerical potentials reasonably well.

with $q \equiv k/[\Omega_0 h^2 \exp(-2\Omega_b)]$ in units of Mpc^{-1} [122, 6]. Note that $q \propto k/k_{eq}$ approximately, reflecting the fact that only modes that cross the Jeans length before equality are suppressed. This implies that the potentials are larger in amplitude if equality occurs later, *i.e.* for high $\Omega_0 h^2$ models. Equation (A.15) therefore empirically accounts for the lack of growth in the radiation-dominated era. Now let us consider the time evolution of the potential. We know that in the matter-dominated epoch the potentials are constant on all scales. Therefore, we smoothly join the superhorizon scale solutions of equation (A.9) with a constant matter-dominated tail whose relative amplitude is given by the transfer function. Since the Jeans crossing epoch is approximately the same as the horizon crossing time in radiation-dominated era, we can take $(k/Ha) \sim ak/k_{eq} \sim 1$ as the matching epoch,

$$\begin{aligned}\Phi(a) &= \bar{\Phi}(a) \left\{ [1 - T(k)] \exp[-\alpha_1 (ak/k_{eq})^\beta] + T(k) \right\}, \\ \Psi(a) &= \bar{\Psi}(a) \left\{ [1 - T(k)] \exp[-\alpha_2 (ak/k_{eq})^\beta] + T(k) \right\},\end{aligned}\tag{A.16}$$

where α_1 , α_2 and β are fitting parameters. We also need a small correction to take into account the free streaming oscillations of the neutrino quadrupole inside the Jeans scale. A very simple approximation can be obtained by making the replacement $\bar{N}_2(a) \rightarrow \bar{N}_2(a) \cos[0.5k/(Ha)]$ in equation (A.9) for $\Psi(a)$. Here the factor 0.5 is a best fit, and the

Hubble parameter $H(a) = (\dot{a}/a)(a_0/a)$. Since it is a higher order correction, this crude approximation is sufficient for our purposes. Comparing this functional form (A.16) with numerical results, we obtain a good fit for $\alpha_1 = 0.11$, $\alpha_2 = 0.097$ and $\beta = 1.6$. In order to calculate the early ISW effect, we take the direct derivative of equations (A.16). In Fig. A.1, we compare these analytic approximations to the numerical results and find good agreement.

A.2 Analytic Construction to 5% Accuracy

A.2.1 Explicit Tight Coupling Solutions

The first step in obtaining the explicit analytic solution for the anisotropy is to calculate the photon fluctuation spectrum at last scattering. We have already seen in §5.2.1 how this may be obtained under the tight coupling approximation once the potential evolution is known. For calculational purposes, it is convenient to express the acoustic solution of equation (5.52) in a more explicit but cumbersome form. One advantage of the analytic tight coupling solutions is they do not require the use of time derivatives of the potentials despite the appearance of equation (5.52). Thus accuracy is not compromised by our lack of a detailed description for $\dot{\Phi}$ and $\dot{\Psi}$. Integrating equation (5.52) by parts twice, we obtain

$$(1 + R)^{1/4}[\hat{\Theta}_0(\eta) + \Phi(\eta)] = [\cos kr_s(\eta) + J(0)\sin kr_s(\eta)] [\Theta_0(0) + \Phi(0)] + I(\eta), \quad (\text{A.17})$$

where the overhat denotes the undamped solution,

$$J(\eta) \equiv -(1 + R)^{3/4} \frac{\sqrt{3}}{k} \frac{d}{d\eta} (1 + R)^{-1/4} = \frac{\sqrt{3}}{4k} \frac{\dot{R}}{\sqrt{1 + R}}, \quad (\text{A.18})$$

and

$$I(\eta) = \frac{k}{\sqrt{3}} \int_0^\eta d\eta' \Phi(\eta') G(\eta') \sin[kr_s(\eta) - kr_s(\eta')], \quad (\text{A.19})$$

with

$$G(\eta) = (1 + R)^{-1/4} \left[1 - (1 + R) \frac{\Psi}{\Phi} + \frac{3}{4k^2} \ddot{R} - J^2 \right]. \quad (\text{A.20})$$

Here we have employed the identity $\dot{\Theta}_0(0) = -\dot{\Phi}(0)$. Since the ISW effect predicts constant $\Theta_0 + \Phi$ at superhorizon scales, we have written these expressions in terms of that quantity.

The dipole solution $\hat{\Theta}_1$ can be similarly obtained from the photon continuity equation $k\Theta_1 = -3(\dot{\Theta}_0 + \dot{\Phi})$,

$$(1+R)^{3/4} \frac{\hat{\Theta}_1(\eta)}{\sqrt{3}} = [1+J(\eta)J(0)][\Theta_0(0) + \Phi(0)]\text{sinc}kr_s(\eta) \\ + [J(\eta) - J(0)][\Theta_0(0) + \Phi(0)]\text{cos}kr_s(\eta) \\ + J(\eta)I(\eta) - \frac{k}{\sqrt{3}} \int_0^\eta d\eta' \Phi(\eta') G(\eta') \text{cos}[kr_s(\eta) - kr_s(\eta')], \quad (\text{A.21})$$

where we have used the relation $\dot{r}_s = c_s = (1/\sqrt{3})(1+R)^{-1/2}$. Notice that we do not need $\dot{\Phi}$ even in the boundary terms in either equation (A.17) and (A.21).

At large scales, $k < 0.08h^3 \text{ Mpc}^{-1}$ this WKB solution fails because the oscillation rate becomes comparable to rate at which the sound speed is changing (see §5.2.1). On the other hand, we know the large scale behavior is given by the dilation effect $\Theta(\eta) = \Theta(0) - \Phi(\eta) + \Phi(0)$. Comparison with (A.17) suggests that an approximate matching onto large scales can be obtained by dropping the explicit R dependence,

$$[\hat{\Theta}_0(\eta) + \Phi(\eta)] = [\Theta_0(0) + \Phi(0)]\text{cos}kr_s(\eta) + \frac{k}{\sqrt{3}} \int_0^\eta d\eta' [\Phi(\eta') - \Psi(\eta')] \text{sin}[kr_s(\eta) - kr_s(\eta')]. \quad (\text{A.22})$$

Here we take the true $R \neq 0$ sound horizon r_s in order to match more smoothly onto the small scale solution. In the CDM model, the error this causes at large scales is minimal. The continuity equation now implies

$$(1+R)^{1/2} \frac{\hat{\Theta}_1(\eta)}{\sqrt{3}} = [\Theta_0(0) + \Phi(0)]\text{sinc}kr_s(\eta) - \frac{k}{\sqrt{3}} \int_0^\eta d\eta' [\Phi(\eta') - \Psi(\eta')] \text{cos}[kr_s(\eta) - kr_s(\eta')]. \quad (\text{A.23})$$

Finally, the following relations are useful for computation:

$$R = \frac{1}{1-f_\nu} \frac{3\Omega_b}{4\Omega_0} a, \quad \dot{R} = \dot{a}R_{eq} = \frac{k_{eq}}{\sqrt{2}} \sqrt{1+a} R_{eq}, \quad \ddot{R} = \frac{1}{4} k_{eq}^2 R_{eq}, \quad (\text{A.24})$$

and recall

$$k_{eq}r_s = \frac{2}{3} \sqrt{\frac{6}{R_{eq}}} \ln \frac{\sqrt{1+R} + \sqrt{R+R_{eq}}}{1 + \sqrt{R_{eq}}}, \quad (\text{A.25})$$

where $R_{eq} \equiv R(\eta_{eq})$ and we have employed the relation $k_{eq}\eta = 2\sqrt{2}(\sqrt{1+a}-1)$. Here $1 + \rho_\nu/\rho_\gamma = (1-f_\nu)^{-1} = 1.68$. Note that a is normalized at equality $a_{eq}/a_0 = a_0^{-1} = 2.38 \times 10^{-5} \Theta_{2.7}^4 (\Omega_0 h^2)^{-1} (1-f_\nu)^{-1}$, and the scale which passes the horizon at equality is $k_{eq} = 1.17/\eta_{eq} = 9.67 \times 10^{-2} \Theta_{2.7}^{-2} \Omega_0 h^2 (1-f_\nu)^{1/2} \text{ Mpc}^{-1}$. Evaluating these expressions at last scattering gives the solution in the absence of diffusion damping. To account for diffusion damping through last scattering, one needs to know the ionization history through recombination.

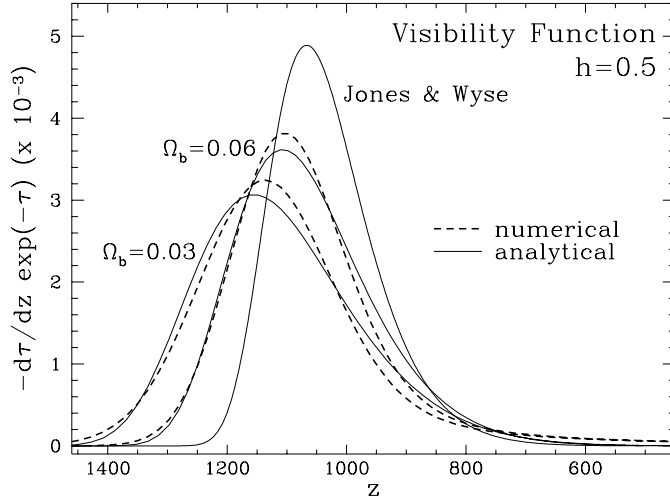


Figure A.2: Visibility Function

The redshift visibility function. Notice that the weak dependence on Ω_b of the visibility function is adequately described by the analytic fitting formula, whereas the Jones & Wyse [91] fitting formula [their equation (23)] does not.

A.2.2 Recombination Revisited

Atomic Considerations

Some care must be taken in calculating the recombination history of hydrogen. In particular, hydrogen recombines more slowly than Saha prediction presented in §6.3.4. Lyman α and Lyman continuum photons from recombination to the ground state immediately reionize another hydrogen atom leaving no net effect. It was realized long ago [123, 183] that net recombination occurs through the forbidden 2-photon decay from the $2s$ level and by the loss of Lyman α photons to the cosmological redshift. The result is that the hydrogen ionization fraction

$$x_H \equiv n_e/n_H = (1 - Y_p)^{-1} n_e/n_b = (1 - Y_p)^{-1} x_e, \quad (\text{A.26})$$

[see equation (3.7)] obeys the differential equation [123],

$$\frac{dx_H}{dt} = C_r [\beta(1 - x_H) - n_H \alpha_B x_e^2], \quad (\text{A.27})$$

where

$$\beta = \left(\frac{m_e k_B T_b}{2\pi \hbar^2} \right)^{3/2} e^{-B_1/k_B T_b} \alpha_B \quad (\text{A.28})$$

is the ionization rate out of the ground state, with the ground state binding energy $B_1 = 13.6\text{eV}$ and

$$\alpha_B = 10^{-13} \frac{aT_4^b}{1 + cT_4^d} \text{cm}^3\text{s}^{-1} \quad (\text{A.29})$$

is the ‘case B’ recombination rate which excludes those to the ground state [129]. Here the fitting constants are $a = 4.309$, $b = -0.6166$, $c = 0.6703$, $d = 0.5300$ with $T_4 = T_b/10^4\text{K}$.

The suppression factor

$$C_r = \frac{\Lambda_\alpha + \Lambda_{2s \rightarrow 1s}}{\Lambda_\alpha + \Lambda_{2s \rightarrow 1s} + \beta e^{h\nu_\alpha/k_B T_b}}, \quad (\text{A.30})$$

takes into account the 2-photon decay rate $\Lambda_{2s \rightarrow 1s} = 8.22458\text{s}^{-1}$ [60] and the hydrogen production rate through redshifting out of the line [123]

$$\Lambda_\alpha = \frac{8\pi}{\lambda_\alpha^3(1 - x_H)n_H} H, \quad \lambda_\alpha = c/\nu_\alpha = \frac{8\pi\hbar c}{3B_1} = 1.216 \times 10^{-5}\text{cm}, \quad (\text{A.31})$$

where recall H is the Hubble parameter. Since helium recombination precedes hydrogen we can assume that at the start of hydrogen recombination $x_e = (1 - Y_p)$ or $x_H = 1$. We shall see below what effect helium recombination has on the spectrum.

From equation (3.8), the baryon temperature evolution is governed by

$$\frac{dT_b}{dt} = -\frac{1}{t_{cool}}(T_b - T) - 2\frac{da}{dt}\frac{1}{a}T_b, \quad (\text{A.32})$$

with

$$t_{cool} = 7.66 \times 10^{19} \frac{(1 + x_e)/2 - (3 + 2x_e)Y_p/8}{1 - Y_p/2} x_e^{-1} \Theta_{2.7}^{-4} (1 + z)^{-4} \text{s}. \quad (\text{A.33})$$

Since this short time scale implies that the electron temperature tracks the photon temperature until late redshifts and low ionization, we can determine its evolution away from the photon temperature iteratively by employing the $T_b = T$ solution for x_e . The two temperatures only start diverging at $z \lesssim 100$ and thus is irrelevant for CMB anisotropies [123, 77]. We can therefore replace the baryon temperature with $T_b = T_0(1 + z)$.

Ionization Fitting Formulae

It is also useful to have fitting formula to the solutions of equation (A.27). The total optical depth from the present to the critical recombination epoch $800 < z < 1200$ can be approximated as

$$\tau(z, 0) \simeq \Omega_b^{c_1} \left(\frac{z}{1000} \right)^{c_2}, \quad (\text{A.34})$$

where $c_1 = 0.43$ and $c_2 = 16 + 1.8 \ln \Omega_b$. Since the range of reasonable values for h is limited to $0.5 \lesssim h \lesssim 0.8$, we have ignored the small h dependence. For definiteness, we take last scattering to occur at z_* where the optical depth $\tau(z_*, 0) = 1$. It immediately follows from (A.34) that this occurs at¹

$$\frac{z_*}{1000} \simeq \Omega_b^{-c_1/c_2} = \Omega_b^{-0.027/(1+0.11 \ln \Omega_b)}, \quad (\text{A.35})$$

which is weakly dependent on Ω_b . The differential optical depth $\dot{\tau}$ then becomes

$$\dot{\tau}(z) = \frac{c_2}{1000} \Omega_b^{c_1} \left(\frac{z}{1000} \right)^{c_2-1} \frac{\dot{a}}{a} (1+z), \quad (\text{A.36})$$

where $\dot{\tau}$ is by definition positive since $\dot{\tau} \equiv d[\tau(\eta', \eta)]/d\eta$. Finally, the ionization fraction is given by $x_e(z) = \dot{\tau} a_0 / n_e \sigma_T a$, where

$$(n_e \sigma_T a / a_0)^{-1} = 4.3 \times 10^4 (1 - Y_p/2)^{-1} (\Omega_b h^2)^{-1} (1+z)^{-2} \text{Mpc}. \quad (\text{A.37})$$

Of course, where the formula (A.36) implies $x_e > 1$, we set $x_e = 1$, *i.e.* $\dot{\tau} = n_e \sigma_T a / a_0$. Or slightly better, impose two step functions: from $x_e = 1$ to $1 - Y_p/2$ at $z = 6000$ and $1 - Y_p$ at $z = 2500$ to account for helium recombination. To the level that we expect the analytic formulae to work, these corrections are insignificant. In Fig. A.2, we show the numerical values for the visibility function in redshift space $-(d\tau/dz)e^{-\tau}$ compared with these analytic fits.

A.2.3 Analytic Results

The decrease in ionization fraction implies an increase in the Compton mean free path and hence the diffusion length. Recall that the damping length is given by

$$k_D^{-2}(\eta) = \frac{1}{6} \int_0^\eta d\eta' \frac{1}{\dot{\tau}} \frac{R^2 + 4(1+R)/5}{(1+R)^2}. \quad (\text{A.38})$$

and fluctuations are damped as $\exp[-(k/k_D)^2]$ assuming $R\Psi \ll \Theta_0$ (see section A.3.1). To account for the evolution after last scattering, note that the Boltzmann equation in flat space has the formal solution

$$[\Theta + \Psi](\eta_0, \mu) = \int_0^{\eta_0} \left\{ [\Theta_0 + \Psi - i\mu V_b] \dot{\tau} - \dot{\Phi} + \dot{\Psi} \right\} e^{-\tau(\eta, \eta_0)} e^{ik\mu(\eta - \eta_0)} d\eta. \quad (\text{A.39})$$

¹A more general expression including variations in $\Omega_0 h^2$ is given in [84]

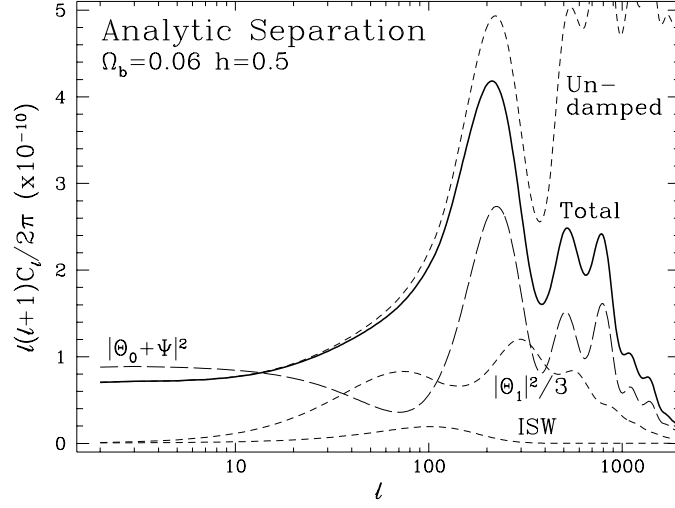


Figure A.3: Analytic Separation of Effects

Individual contributions to the anisotropy in the CDM model. At the largest scales ($\ell \lesssim 30$), the monopole $|\Theta_0 + \Psi|$ from the ordinary Sachs-Wolfe effect dominates. The 20% correction from the early ISW effect on scales larger than the first Doppler peak appears misleadingly small in power (see text). The ordinary Sachs-Wolfe effect is overpowered by the acoustic oscillations at small scales leading to a deficit at intermediate scales ($\ell \sim 70$) which is filled in by the adiabatic dipole Θ_1 and the ISW effect. Although the dipole cannot be neglected, the monopole is clearly responsible for the general structure of the Doppler peaks. Diffusion damping significantly reduces fluctuations beyond the first Doppler peak and cuts off the anisotropies at $\ell \sim 1000$.

For sufficiently large scales, we can take the slowly varying quantities out of this integral. Thus accounting for diffusion damping, the fluctuations at last scattering become $[\Theta_0 + \Psi](\eta_*) = [\hat{\Theta}_0 + \Psi](\eta_*)\mathcal{D}(k)$ and $\Theta_1(\eta_*) = \hat{\Theta}_1(\eta_*)\mathcal{D}(k)$, where

$$\mathcal{D}(k) = \int_0^{\eta_0} \dot{\tau} e^{-\tau(\eta, \eta_0)} e^{-[k/k_D(\eta)]^2} d\eta. \quad (\text{A.40})$$

Taking the multipole moments and setting $V_b = \Theta_1$, we find for $\ell \geq 2$,

$$\begin{aligned} \Theta_\ell(\eta_0) \simeq & [\Theta_0 + \Psi](\eta_*) (2\ell + 1) j_\ell(k\Delta\eta_*) + \Theta_1(\eta_*) [\ell j_{\ell-1}(k\Delta\eta_*) - (\ell + 1) j_{\ell+1}(k\Delta\eta_*)] \\ & + (2\ell + 1) \int_{\eta_*}^{\eta_0} [\dot{\Psi} - \dot{\Phi}] j_\ell(k\Delta\eta) d\eta. \end{aligned} \quad (\text{A.41})$$

Integrating over all k modes of the perturbation, we obtain

$$\frac{2\ell + 1}{4\pi} C_\ell = \frac{V}{2\pi^2} \int \frac{dk}{k} \frac{k^3 |\Theta_\ell(\eta_0, k)|^2}{2\ell + 1}. \quad (\text{A.42})$$

This completes the explicit construction of the anisotropy spectrum.

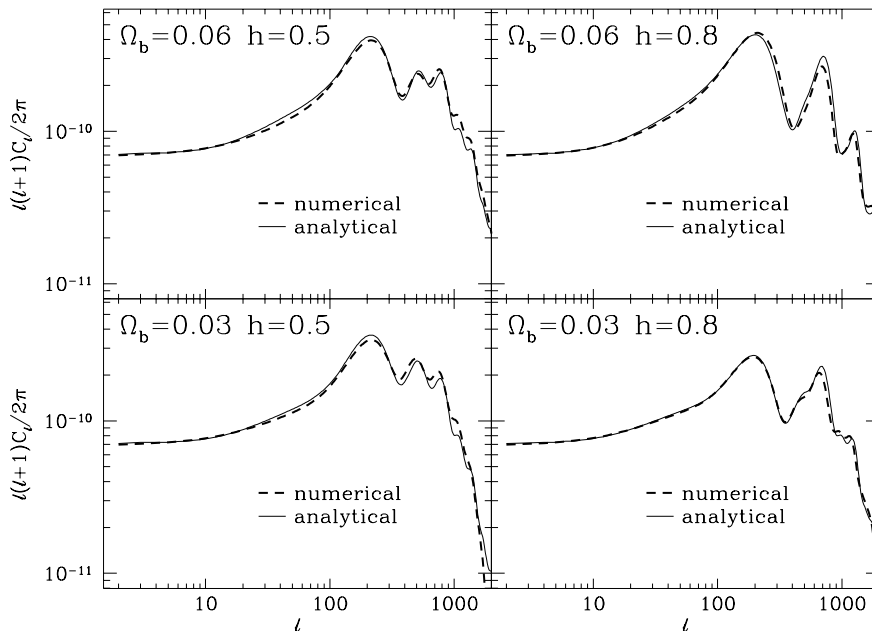


Figure A.4: Comparison of Analytic and Numerical Results

The agreement between analytic and numerical results is excellent on all scales.

In Fig. A.3, we show the analytic decomposition of the spectrum into the effective temperature perturbation at last scattering $[\Theta_0 + \Psi](\eta_*)$, the dipole or Doppler term $\Theta_1/\sqrt{3}$, the early ISW effect and diffusion damping. Notice that without diffusion damping the dilation boost of the acoustic oscillations for small scales that enter during radiation domination is clearly evident. The early ISW effect appears misleadingly small in power. In fact it adds coherently with the SW effect, whereas the dipole roughly adds in quadrature. The 20% shift in power spectrum normalization from the monopole-only solution is entirely due to the 1% ISW effect. Finally let us compare the analytic construction with the full numerical results (see Fig. A.4). The analytic approximation agrees at the 5% level to the damping scale for the range of parameters accessible to the CDM model. By extending the analysis in this section to other models, comparable accuracy can be obtained.

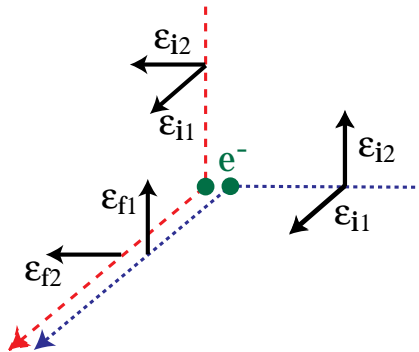


Figure A.5: Polarization Generation

A quadrupole moment in the temperature distributions sources polarization. Unless the temperature or mean energy of the radiation at ninety degree angles is the same, polarization dependent preferential scattering will cause more intensity in one polarization than the other in the outgoing scattered radiation. Reversing the arrow of time, we see that linear polarization sources a quadrupole anisotropy. The length of the dashes represents the wavelength of the photon.

A.3 Toward 1% Accuracy

The next generation of space based CMB anisotropy experiments have the potential to measure all the C_ℓ 's out to $\ell \sim 500$ to the cosmic variance limit (*i.e.* accuracy $\ell^{-1/2}$). In this case, the amount of information which may be retrieved from the CMB is truly enormous. If the inflationary CDM cosmology turns out to be correct, there is even a possibility that we can probe the physics of inflation through tensor contributions (see *e.g.* [168, 47]) and the shape of the initial power spectrum. A small difference between C_ℓ 's for neutrinos with an eV scale mass and the standard massless case appears near the damping scale and provides the possibility of an indirect measure of the neutrino mass through anisotropies. To realize these goals, we must understand the spectrum at the 1% level. Many secondary effects like those discussed in §7 can contribute at this level. As a first step toward the goal of 1% accuracy, it is also necessary to refine calculations of primary anisotropies. The following discussion draws results from [77].

A.3.1 Polarization Damping

The quadrupole moment of the temperature distribution leads to linear polarization in the microwave background (*e.g.* [135, 93]) and vice versa [16]. The precise level

of the temperature anisotropies therefore is not recovered by neglecting polarization. The Thomson cross section depends on angle as $|\epsilon_f \cdot \epsilon_i|^2$, where ϵ_f and ϵ_i are the final and initial polarization vectors respectively [16, 93]. A quadrupole temperature anisotropy therefore sources polarization (see Fig. A.5). Reversing the arrow of time, polarization also feeds back to generate a temperature quadrupole.

To formally account for polarization, a separate Boltzmann hierarchy is added for the temperature perturbation Θ^Q in the Stokes parameter Q [16, 103],

$$\begin{aligned}\dot{\Theta}_0^Q &= -\frac{k}{3}\Theta_1^Q - \dot{\tau} \left[\frac{1}{2}\Theta_0^Q - \frac{1}{10}(\Theta_2 + \Theta_2^Q) \right], \\ \dot{\Theta}_1^Q &= k \left[\Theta_0^Q - \frac{2}{5}K_2^{1/2}\Theta_2^Q \right] - \dot{\tau}\Theta_1^Q, \\ \dot{\Theta}_2^Q &= k \left[\frac{2}{3}K_2^{1/2}\Theta_1^Q - \frac{3}{7}K_3^{1/2}\Theta_3^Q \right] - \dot{\tau} \left(\frac{9}{10}\Theta_2^Q - \frac{1}{10}\Theta_2 - \frac{1}{2}\Theta_0^Q \right), \\ \dot{\Theta}_\ell^Q &= k \left[\frac{\ell}{2\ell-1}K_\ell^{1/2}\Theta_{\ell-1}^Q - \frac{\ell+1}{2\ell+3}K_{\ell+1}^{1/2}\Theta_{\ell+1}^Q \right] - \dot{\tau}\Theta_\ell^Q, \quad (\ell > 2)\end{aligned}\tag{A.43}$$

where recall $K_\ell = 1 - (\ell^2 + 1)K/k^2$ and goes to unity if $K = 0$. Notice that as expected, it is the temperature quadrupole that sources monopole and quadrupole polarization perturbations. Since the temperature quadrupole itself is suppressed in the tight coupling limit, we expect that polarization will yield only a higher order correction for primary anisotropies. Polarization feeds back to modify the quadrupole equation of the temperature hierarchy (4.54)

$$\dot{\Theta}_2 = k \left[\frac{2}{3}K_2^{1/2}\Theta_1 - \frac{3}{7}K_3^{1/2}\Theta_3 \right] - \dot{\tau} \left(\frac{9}{10}\Theta_2 - \frac{1}{10}\Theta_2^Q - \frac{1}{2}\Theta_0^Q \right).\tag{A.44}$$

Other multipole moments of the temperature hierarchy remain unmodified.

It is easy to see what effect polarization has on anisotropies. Let us expand these equations in the Compton scattering time $\dot{\tau}^{-1}$. The polarization monopole $\ell = 0$ and quadrupole $\ell = 2$ equations together imply that

$$\Theta_2^Q = \Theta_0^Q = \frac{1}{4}\Theta_2.\tag{A.45}$$

Putting these relations into equation (A.44) for the feedback effect, we see that it changes the Compton coupling quadrupole coefficient from $\frac{9}{10} \rightarrow \frac{3}{4}$. This affects the damping rate of acoustic oscillations as we shall now show.

Diffusion damping occurs to second order in the tight coupling expansion of the photon dipole and baryon Euler equations [see equations (4.54), (4.58)],

$$\Theta_1 - V_b = \dot{\tau}^{-1} \left[k(\Theta_0 + \Psi) - \frac{2}{5}k\Theta_2 - \dot{\Theta}_1 \right],\tag{A.46}$$

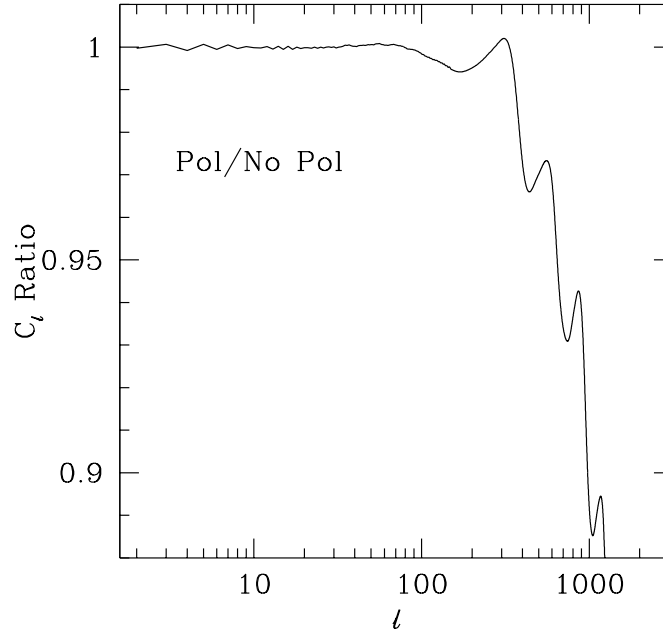


Figure A.6: Polarization Damping

The ratio of C_ℓ for a standard CDM model where polarization is explicitly followed, relative to a calculation where it is neglected. Polarization increases the damping scale of temperature anisotropies. Calculations courtesy of M. White [77].

$$\Theta_1 - V_b = \dot{\tau}^{-1} R[\dot{V}_b + \frac{\dot{a}}{a} V_b - k\Psi] \quad (\text{A.47})$$

where we have assumed that $K/k^2 \ll 1$. Notice that a quadrupole generated to first order in $\dot{\tau}^{-1}$ affects the evolution of the dipole to second order. To lowest order, equation (A.44) gives the quadrupole source as

$$\Theta_2 = \dot{\tau}^{-1} f_2^{-1} \frac{2}{3} k \Theta_1, \quad (\text{A.48})$$

where we have left the effect of polarization and the angular dependence of Compton scattering implicit in

$$f_2 = \begin{cases} 9/10 & \text{angular dependence} \\ 3/4. & \text{polarization} \end{cases} \quad (\text{A.49})$$

The photon continuity or monopole equation yields

$$\dot{\Theta}_0 = -\frac{k}{3} \Theta_1 - \dot{\Phi}. \quad (\text{A.50})$$

To solve these equations to second order in $\dot{\tau}^{-1}$, let us assume a solution of the form $\Theta_1 \propto \exp i \int \omega d\eta$ and ignore variations on the expansion time scale compared with those at

the frequency of oscillation. The electron velocity, obtained by iteration is to second order

$$V_b = \Theta_1 - \dot{\tau}^{-1} R [i\omega\Theta_1 - k\Psi] - \dot{\tau}^{-2} R^2 \omega^2 \Theta_1. \quad (\text{A.51})$$

Substituting this into the dipole equation (A.46) and eliminating the zeroth order term yields

$$i\omega(1+R)\Theta_1 = k[\Theta_0 + (1+R)\Psi] - \dot{\tau}^{-1} R^2 \omega^2 \Theta_1 - \frac{4}{15} \dot{\tau}^{-1} f_2^{-1} k^2 \Theta_1. \quad (\text{A.52})$$

The combination $\Theta_0 + (1+R)\Psi$ was shown in §5.2.2 to oscillate acoustically around zero under the assumption of a slowly varying R . This is because of the baryonic infall contribution $R\Psi$ and the photon blueshift Ψ which displaces the zero point. It is therefore natural to try a solution where $\Theta_0 + (1+R)\Psi \propto \exp i \int \omega d\eta$, since its oscillations should match with the dipole. Note also that after diffusion damping, the photon temperature retains a contribution of order $R\Psi$ due to baryonic infall.

Employing this relation in the photon continuity equation and ignoring slow changes in R , Φ and Ψ yields the dispersion relation

$$(1+R)\omega^2 = \frac{k^2}{3} + i\dot{\tau}^{-1}\omega \left(R^2\omega^2 + \frac{4}{15}k^2 f_2^{-1} \right). \quad (\text{A.53})$$

Using the lowest order solution to rewrite $\omega^3 = k^2\omega/3(1+R)$ and solving the resultant quadratic equation, we obtain [93]

$$\omega = \pm \frac{k}{\sqrt{3(1+R)}} + \frac{i}{6} k^2 \dot{\tau}^{-1} \left[\frac{R^2}{(1+R)^2} + \frac{4}{5} f_2^{-1} \frac{1}{1+R} \right]. \quad (\text{A.54})$$

In other words, the oscillations damp as $\exp[-(k/k_D)^2]$ and the damping length becomes

$$k_D^{-2} = \frac{1}{6} \int d\eta \frac{1}{\dot{\tau}} \frac{R^2 + 4f_2^{-1}(1+R)/5}{(1+R)^2}. \quad (\text{A.55})$$

In the photon-dominated $R \ll 1$ limit, the damping length increases by 5% ($f_2 = \frac{9}{10}$) through the angular dependence of Compton scattering and an additional 10% through polarization ($f_2 = \frac{3}{4}$). Closer to baryon domination, the effect of f_2 is less noticeable. Qualitatively, the polarization sources the quadrupole and generates viscosity which is then dissipated [93]. Actual numerical results of the effect of polarization are shown in in Fig. A.6 and are in good agreement with these analytic estimates of the relative effect. The fractional difference at small scales can be quite significant due to the near exponential behavior of damping.

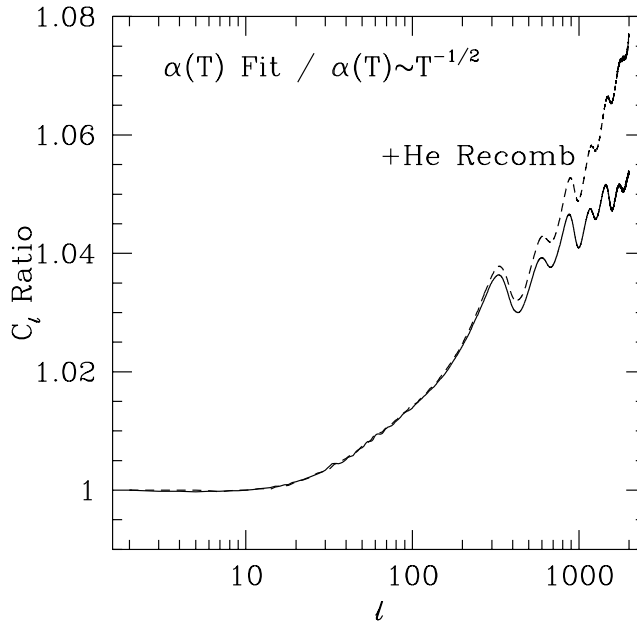


Figure A.7: Helium Recombination

Ionized helium at high redshift contributes free electrons to oppose photon diffusion and thus even at recombination has a small effect in decreasing the damping scale. Also shown here is the effect of improving the fitting formula for the ‘case B’ recombination coefficient α_B of equation (A.29) from the $T^{-1/2}$ scaling of [123]. Calculations courtesy of M. White [77].

A.3.2 Helium Recombination

One might naively expect helium recombination to have a negligible effect on the C_ℓ ’s because helium recombines while the radiation and matter are still very tightly coupled, at $z \simeq 2500$ for singly ionized and $z \simeq 6000$ for doubly ionized helium. However the diffusion damping length grows continuously and is sensitive to the full thermal history. Inclusion of helium recombination affects the 2nd, 3rd and 4th peaks at the 0.2%, 0.4% and 1% levels, as shown in Fig. A.7. Hence it *is* important to follow the recombination of the helium in order to obtain accurate C_ℓ ’s at the percent level. Note that because of atomic collisions, helium atoms are tightly coupled to the hydrogen through collisions even after helium recombination, Since they contribute to the inertia of the photon-baryon fluid, helium atoms should be kept in the baryon evolution equations. It has been shown that simple use of the Saha equation for helium is as accurate as treating helium atoms more fully [77]. The trace of neutral hydrogen, present even at redshifts $z \simeq 2500$, can absorb

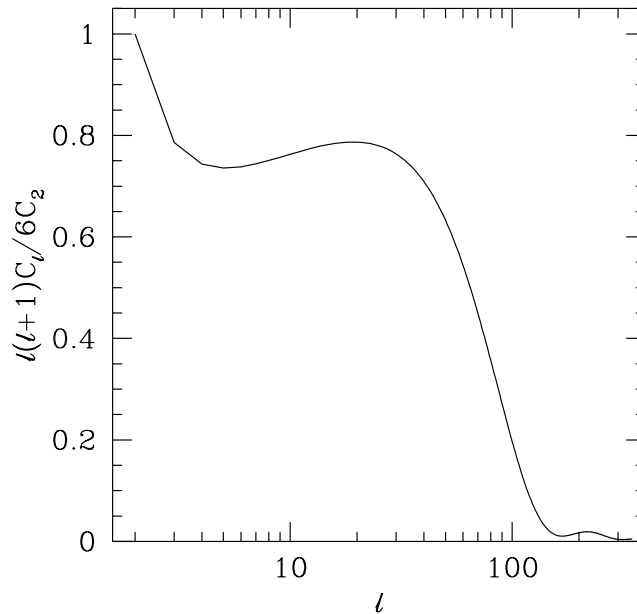


Figure A.8: Gravity Wave Spectrum

A flat spectrum of tensor generated anisotropies with for standard CDM $\Omega_0 = 1.0$, $h = 0.5$, $\Omega_b = 0.05$ $n_T = 1$. The tensor and scalar spectrum add in quadrature. Calculation courtesy of M. White [77].

the helium Ly α photons. This prevents helium recombination photons from ionizing other helium atoms, unlike their hydrogen counterparts.

A.3.3 Gravity Waves

In addition to the scalar modes with which the previous discussion has been involved, there is the possibility that inflation excites tensor (*i.e.* gravity wave) perturbations as well [154]. Early work on tensors and the CMB was performed by [155, 54, 4, 155]. There exist several semi-analytic approximations of varying accuracy, the most recent and accurate being due to [1]. To calculate the tensor spectrum numerically one uses the formalism of [132] as first worked out in detail by [37]. This leads to another set of Boltzmann equations, independent of those for the scalars, which follow the temperature and polarization anisotropies of the tensors. The final result is then $C_\ell^{(\text{tot})} = C_\ell^{(S)} + C_\ell^{(T)}$ where the relative normalization of the tensor and scalar components depends on the details of the perturbation generation scenario. In Fig. A.8, we plot the tensor contribution $C_\ell^{(T)}$, for a model with the parameters of standard CDM.

The qualitative features of this spectrum are easy to understand. The CMB couples to gravity waves through its quadrupole moment. The amplitude of the metric perturbation induced by a gravity wave h_ϵ , where ϵ represents the two possible polarizations, evolves as

$$\ddot{h}_\epsilon + 2\frac{\dot{a}}{a}\dot{h}_\epsilon + (k^2 + 2K)h_\epsilon = 8\pi G \left(\frac{a}{a_0}\right)^2 p_T \Pi_T^{(2)} \quad (\text{A.56})$$

(see [99] eqn. 4.15) where $\Pi_T^{(2)}$ is the *tensor* contribution to the anisotropic stress. Ignoring the feedback effect through the radiation quadrupoles, this is a damped oscillator equation. Inflation predicts a spectrum of initial gravity waves $k^3|h_\epsilon(0, k)|^2 \propto k^{n_T-1}$. For these initial conditions, h_ϵ remains constant outside the horizon and feels the k^2 “pressure” force near horizon crossing. The consequent changes in h_ϵ are damped by the expansion. Since $\dot{a}/a = \eta^{-1}$ in the radiation-dominated epoch and $2\eta^{-1}$ in the matter-dominated epoch, gravity waves are damped less rapidly in the former [$j_0(k\eta)$] than in the latter [$j_1(k\eta)/k\eta$].

Just like changes in the scalar spatial metric perturbation Φ , \dot{h}_ϵ sources radiation perturbations through dilation from the stretching of space. The difference is that due to the spin two nature of gravity waves, the deformation sources a quadrupole rather than a monopole fluctuation in the matter. This makes its effects unimportant for density perturbations and structure formation. Contributions to the photon temperature perturbation before last scattering are rapidly damped away by Compton isotropization. However during the free streaming epoch, the quadrupole source like the monopole projects onto higher multipoles as the photons free stream, causing anisotropies in the CMB through the ISW effect. This explains the three prominent features in the spectrum of Fig. A.8. Modes that cross the horizon recently source mainly the quadrupole, boosting the low order multipoles. Smaller scales experience the full decay of h_ϵ , leading to a small rise. However the smallest scales contribute negligibly since they enter the horizon before last scattering. Since these are exactly the scales on which acoustic oscillations appear, it is very likely that gravity waves are unimportant for small angle anisotropies. On the other hand, the ratio of large to small scale anisotropies may tell us something about the relative amplitude of the tensor to scalar initial contributions [168, 47].

A.3.4 Massive Neutrinos

The radiation content determines the amount of dilation boost the acoustic modes encounter at horizon crossing from the decay of the potential. Lowering the radiation

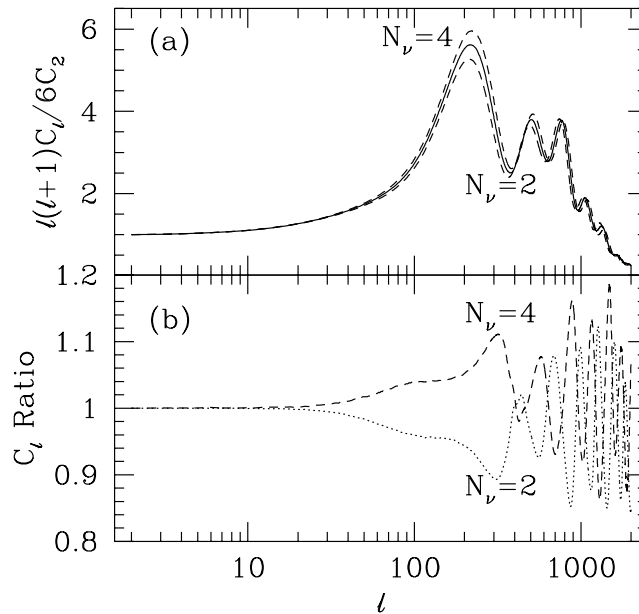


Figure A.9: Number of Massless Neutrinos

Relativistic neutrinos increase the amount of dilation boost from the potential decay that the acoustic mode encounters at horizon crossing. The prediction for massive neutrino models depends on when the neutrinos become non-relativistic. For a mass of a few eV, the horizon at this epoch projects onto $\ell \sim 500$ and the resultant spectrum will be a smooth transition from $N_\nu = 3$ to $N_\nu = 2$ near this scale. Calculation courtesy of M. White [77].

content lowers the boost. Thus the CMB is sensitive to the number of effectively massless neutrino families N_ν before last scattering (see Fig. A.9). Massive neutrinos are a promising dark matter candidate and can solve some of the problems CDM models have with large scale structure formation [42, 97]. By assuming a neutrino with a few eV mass and composing the rest of the critical density with cold dark matter, one retains many of the features of the CDM model while also lowering the excess of small scale power. A low mass neutrino is relativistic when a galaxy-sized mass enters the horizon. Thus neutrino free streaming will collisionlessly damp power on these scales. However for the degree and larger scales that the current CMB experiments probe, such neutrinos are already non-relativistic at horizon crossing and leave the same signature as CDM. The transition scale is around $\ell \simeq 500$ for a neutrino mass of a few eV. Thus the CMB anisotropy spectrum should follow the $N_\nu = 3$ CDM prediction until roughly those scales and then decrease to the lower N_ν prediction. Extracting the neutrino mass will therefore require a detailed understanding of the damping

tail and any secondary and foreground contributions – an extremely challenging, but not unthinkable task.